

1 Possible linkage between winter extreme low temperature over  
2 central-western China and autumn sea ice loss

3  
4 **Shuoyi Ding**<sup>1,2,3</sup>, **Bingyi Wu**<sup>1,3,#</sup>, **Wen Chen**<sup>4,2</sup>, **Hans-F. Graf**<sup>5,6</sup>, **Xuanwen**  
5 **Zhang**<sup>1,3,7</sup>

6 <sup>1</sup>Department of Atmospheric and Oceanic Sciences, and Institute of Atmospheric  
7 Sciences, Fudan University, Shanghai, China.

8 <sup>2</sup>State Key Laboratory of Numerical Modeling for Atmospheric Sciences and  
9 Geophysical Fluid Dynamics, Institute of Atmospheric Physics, Chinese Academy of  
10 Sciences, Beijing, China

11 <sup>3</sup>CMA-FDU Joint Laboratory of Marine Meteorology, Shanghai, China.

12 <sup>4</sup>Department of Atmospheric Science, Yunnan University, Kunming 650500, China

13 <sup>5</sup>Centre for Atmospheric Science, University Cambridge, Cambridge, UK

14 <sup>6</sup>Hommel&Graf Environmental, Goettingen, Germany

15 <sup>7</sup>School of Atmospheric Sciences, Chengdu University of Information Technology,  
16 Chengdu

17 #Corresponding author: Bingyi Wu ([bywu@fudan.edu.cn](mailto:bywu@fudan.edu.cn))

18  
19 **Key Points:**

20 Autumn EsCB sea ice loss favors cold air east of Novaya Zemlya invading western-  
21 central China, thus more frequent extreme low temperature

22 Synoptic eddy-mean flow interaction and anomalous upward planetary wave 2 provide  
23 favorable anticyclonic anomaly for extreme events outburst

24 Intra-seasonal downward propagated stratospheric anomalies are vital for the Ural  
25 anticyclonic anomaly to develop downstream within 7 days

26

27

28

29

30 **Abstract**

31 Based on reanalysis datasets and sea-ice sensitivity experiments, this study has pointed  
32 out that the autumn sea ice loss in East Siberian-Chukchi-Beaufort (EsCB) Seas  
33 significantly increases the frequency of winter extreme low temperature over western-  
34 central China. Autumn sea ice loss warms the troposphere and generates anticyclonic  
35 anomaly over the Arctic region one month later. Under the effects of synoptic eddy-  
36 mean flow interaction and anomalous upward propagated planetary wave 2, the Arctic  
37 anticyclonic anomaly strengthens and develops toward Greenland-Northern Europe,  
38 accompanied by a weakened stratospheric polar vortex. In winter, following intra-  
39 seasonal downward propagation of stratospheric anomalies, the Northern European  
40 positive geopotential anomalies enhance and expand downstream within 7 days,  
41 favoring Arctic cold air east of Novaya Zemlya southward (hyperpolar path)  
42 accumulating in Siberia around Lake of Baikal. In the subsequent 2~3 days, these cold  
43 anomalies rapidly intrude western-central China and induce abrupt sharp cooling, thus  
44 more frequent extreme low temperature there.

45

46 **Plain Language Summary**

47 Arctic sea ice change not only regulates the local ecosystem but extends its influences  
48 into mid- even low- latitudes through several complicated physical processes. Sea ice  
49 variation in EsCB Seas exhibits an increased amplitude and more crucial role in climate  
50 change under global warming. The new findings hinted that autumn EsCB sea ice  
51 decrease would significantly promote western-central China to experience more  
52 frequent winter extreme low temperature. In responses, an Arctic anticyclonic anomaly  
53 occurs one month later and develops toward Greenland-Northern Europe due to  
54 synoptic eddy-mean flow interaction. Enhanced upward propagated planetary wave 2  
55 and associated wave-mean flow interaction maintains the tropospheric Arctic  
56 anomalies and weakens the stratospheric polar vortex. When entering winter, following  
57 intra-seasonal downward propagated stratospheric anomalies, the Northern European  
58 anticyclonic anomaly strengthens downstream within 7 days, favoring favors Arctic  
59 cold air east of Novaya Zemlya rapidly invading western-central China (hyperpolar

60 path) and sudden sharp cooling. Our results have understood how autumn EsCB sea ice  
61 loss contributes to extreme low temperature in China, including possible physical  
62 mechanisms and cold air pathways, unlike previous work focusing on Barents-Kara  
63 Seas and winter-mean temperature change. It provides a new factor and theoretical  
64 foundations for predicting winter extreme low temperature in China.

65

## 66 **1. Introduction**

67 In recent decades, following the rapid Arctic warming and continuous Arctic sea  
68 ice reduction, the Arctic-midlatitude association and possible mechanisms became one  
69 of the focus in climate variability research (Cohen et al., 2020). Arctic sea ice change  
70 and its interaction with the atmosphere (Cohen et al., 2020; Deng and Dai, 2022; Wu et  
71 al., 2022) not only impact the local thermal and dynamic states but also influence mid-  
72 and even low latitudes through complex interactions and feedback processes (Deser et  
73 al., 2004; Honda et al., 2009; Petoukhov and Semenov, 2010; Francis and Vavrus, 2012;  
74 Vihma, 2014; Wu et al., 2017; Screen et al., 2018; Nakamura et al., 2019; Siew et al.,  
75 2020; Cohen et al., 2021). Barents-Kara (BK) Seas are the main region of interest in  
76 many previous studies that showed autumn and winter sea ice loss favor increased  
77 blocking, a strengthened Siberian high, and significant cooling over northern Eurasia  
78 during winter (Francis et al., 2009; Honda et al., 2009; Wu et al., 2011; Mori et al., 2015,  
79 2019; Cohen et al., 2021). The possible mechanisms include weakened high-latitude  
80 westerly winds due to the decreased meridional temperature gradient (Francis and  
81 Vavrus, 2012, 2015) and horizontal or vertical propagation of quasi-stationary planetary  
82 waves (Honda et al., 2009; Zhang et al., 2018a, b). In addition, enhanced meridional  
83 fluctuation of winter atmospheric circulation and stronger quasi-stationary planetary  
84 waves are a result of reduced autumn Arctic sea ice. This leads to persistent weather  
85 patterns and increased frequency of extreme weather events (Francis and Vavrus, 2012,  
86 2015; Tang et al., 2013; Wu et al., 2013, 2017; Overland et al., 2021; Zhang et al. 2022).

87 However, uncertainty remains regarding the Arctic-midlatitude association due to  
88 insignificant or weak atmospheric responses to sea ice reduction in large ensembles of  
89 numerical experiments (Barnes, 2013; Chen et al., 2016a; Sun et al., 2016; Blackport  
90 et al., 2019, 2020, 2021; Cohen et al., 2020). The climate effects of sea ice anomalies  
91 may be obscured by the chaotic nature of the atmosphere (Overland et al., 2021). Some  
92 modeling studies even concluded that winter Eurasian cooling or extreme cold events

93 are simply due to internal atmospheric variability because of very weak and  
94 insignificant simulated atmospheric responses to Arctic sea ice forcing (McCusker et  
95 al., 2016; Koenig et al., 2019). The non-stationary Arctic-midlatitude association due  
96 to global warming induces additional uncertainty. For instance, the climatological sea  
97 ice northward shift, the impact of autumn Arctic sea ice loss on the winter Siberian high  
98 is weakened (Chen et al., 2021). With continuous sea ice loss, the linkage between the  
99 Arctic and Eurasia exhibits a strong low-frequency fluctuation of warm Arctic-cold  
100 Eurasia and warm Arctic-warm Eurasia (Wu et al., 2022). The high sensitivity of mid-  
101 high latitudinal atmospheric responses to the geographical location of Arctic sea ice  
102 anomalies and evident differences in climate effects between regional and entire Arctic  
103 sea ice change also leads to diversity and uncertainty in previous numerical studies  
104 (Chen et al., 2016b; Screen, 2017; Cohen et al., 2020).

105 Recent studies pointed out that autumn sea ice of the East Siberian-Chukchi-  
106 Beaufort (EsCB) Seas exhibits an increased interannual variability under global  
107 warming, and the sea ice loss probably leads to colder northern Eurasia in the  
108 subsequent early winter and early spring (Ding et al., 2021; Ding and Wu, 2021). A  
109 persistent Arctic anticyclonic anomaly, contributed by anomalous upward propagating  
110 quasi-stationary planetary waves and the associated convergence anomaly in the  
111 troposphere and the stratosphere, partly explains the cross-seasonal impacts of autumn  
112 regional sea ice. These studies discussed the Arctic-midlatitude association from the  
113 perspective of seasonal means, similar as most previous works about BK sea ice change  
114 (Wu et al., 2011; Zhang et al., 2018a, b; Cohen et al., 2021).

115 Although the winter mean Eurasian cooling associated with reduced EsCB sea ice  
116 is weak and marginally significant (Figure 1a; Ding et al., 2021), especially for East  
117 Asia/China there is a possibility of short term high impact events. The related  
118 atmospheric anomalies are favorable for rapid and severe cold air outbreaks invading  
119 East Asia/China and contributing to extreme low temperatures. Therefore, this study  
120 will investigate whether the autumn (September-October) sea ice loss over the EsCB  
121 Seas affects the frequency of winter extreme low temperature events over East  
122 Asia/China and will explore the mechanisms of such cold air outbreaks. For this  
123 purpose, we use statistical diagnosis of observations and sea-ice sensitivity model  
124 experiments.

125

## 126 **2. Data and Methodology**

127 Atmospheric monthly and daily mean variables are taken from the NCEP-DOE  
 128 Reanalysis II with 2.5° longitude/latitude resolution, including air temperature,  
 129 geopotential height and horizontal winds (Kanamitsu et al., 2002). The Monthly mean  
 130 sea ice concentration (SIC) with a horizontal resolution of 1.0° × 1.0° comes from the  
 131 Met Office Hadley Center (Rayner et al., 2003). The study period covers 42 winters  
 132 from January 1979 to December 2021. All variables are linearly detrended. We obtain  
 133 similar conclusions using the raw data (not shown).

134 The definition of an extreme low temperature day is the daily-mean air  
 135 temperature (1000 hPa) lower than the 10th percentile of historical records or control  
 136 experiments, and the sum of extreme days during winter represents the frequency of  
 137 extreme low temperature. Western-central China experiencing more than one extreme  
 138 low temperature day is recorded as an extreme event. The interval between two events  
 139 should be longer than 15 days. There are 12 observed (Table S1) and 185 simulated  
 140 extreme low temperature events in low SIC years. We mainly focus on the regional sea  
 141 ice loss in the EsCB Seas (Figure S1a, b) because of its increasing variability (Figure  
 142 S1c, d), and the area-mean SIC anomalies (70.5°N–82.5°N, 135.5°E–119.5°W),  
 143 multiplying by -1.0, are denoted as the EsCB index (Ding et al., 2021). Regression  
 144 analysis is the primary method to explore the observed association between the  
 145 frequency of extreme low temperature over central-western China and autumn EsCB  
 146 sea ice loss. Geopotential height tendency is utilized to portray the feedback of the  
 147 synoptic-scale eddy to the low-frequency flow (Lau and Holopainen, 1984; Lau, 1988;  
 148 Lau and Nath, 1991; Cai et al., 2007). Here, the eddy heat flux term associated with  
 149 baroclinic processes is much smaller (Lau and Holopainen, 1984; Lau and Nath, 1991),  
 150 so we only calculate the eddy vorticity flux term associated with barotropic processes  
 151 is calculated as follows (Cai et al., 2007):

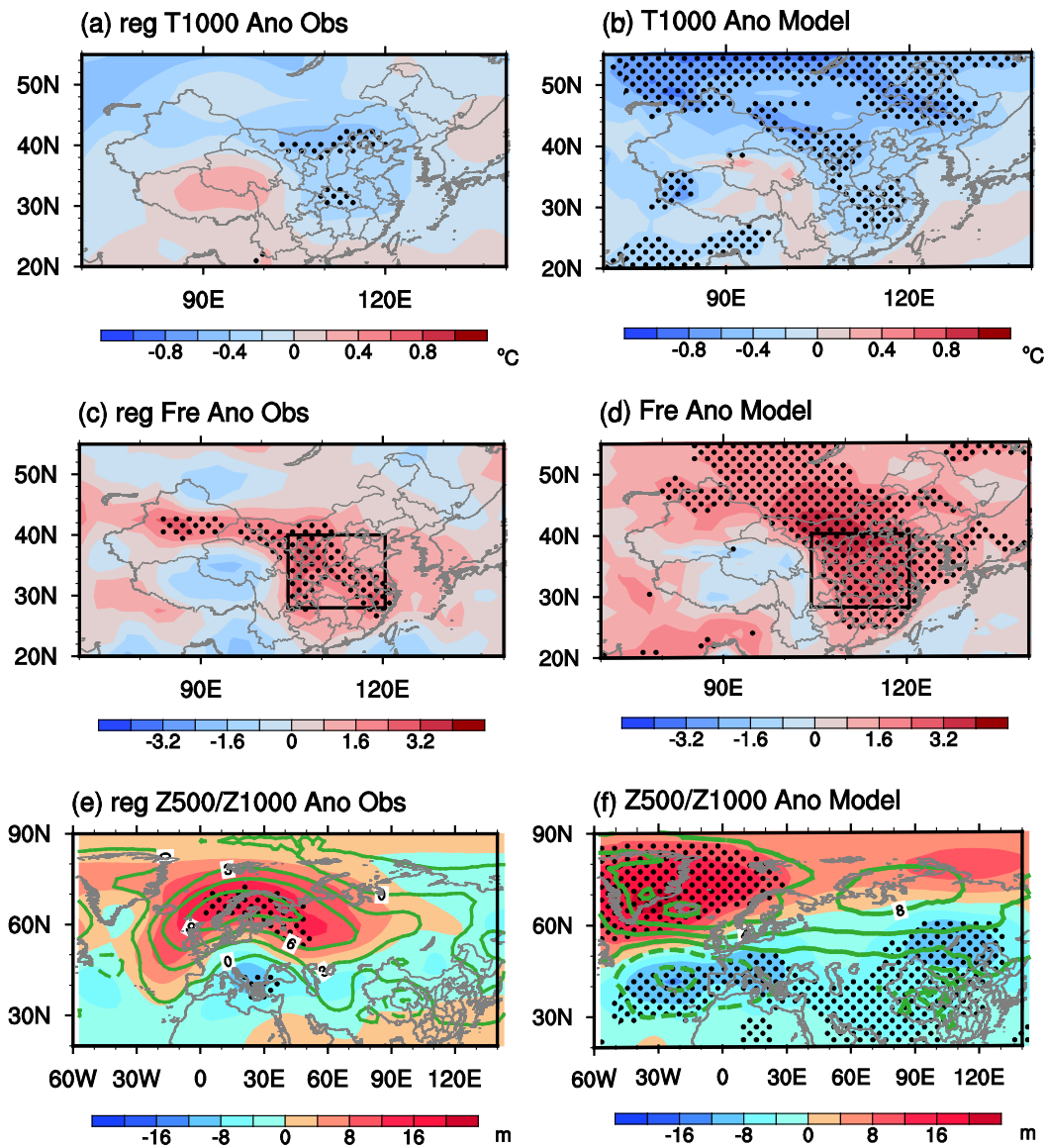
$$152 \quad F = \nabla^{-2} \left[ -\frac{f}{g} \overline{\nabla \cdot \vec{V}'} \zeta' \right]$$

153 where  $\vec{V}'$  and  $\zeta'$  respectively denote the synoptic-scale horizontal winds and relative  
 154 vorticity, derived from a Butterworth band-pass filter with 2-10 day periods.  $\nabla^{-2}$  is  
 155 inverse Laplacian,  $\nabla$  is divergence,  $f$  is the Coriolis parameter and  $g$  is the acceleration

156 of gravity. We also employ the EP flux ( $F_y = -\rho a \cos \varphi \overline{u'v'}$ ,  $F_z = \rho a \cos \varphi \frac{Rf}{HN^2} \overline{v'T'}$ )  
157 and its divergence ( $D_F = \frac{\nabla \cdot \vec{F}}{\rho a \cos \varphi}$ ) to depict the vertical propagation of quasi-stationary  
158 planetary wave activity and the wave-mean flow interaction, respectively (Edmon et al.,  
159 1980; Plumb, 1985). Here,  $F_z$  ( $F_y$ ) is the vertical (meridional) component,  $\rho$  is the air  
160 density,  $a$  is the radius of the earth,  $\varphi$  is the latitude,  $R$  is the gas constant,  $f$  is the  
161 Coriolis parameter,  $H$  is the scale height,  $N$  is buoyancy frequency calculated from the  
162 temperature data,  $u$  is zonal wind,  $v$  is meridional wind and  $T$  is temperature. The primes  
163 and overbars respectively denote zonal deviation and zonal average. The convergence  
164 (divergence) of EP flux leads to decelerated (accelerated) westerly winds (Edmon et al.,  
165 1980; Chen et al., 2002, 2003).

166 The Specified Chemistry Whole Atmosphere Community Climate Model version  
167 4.0 (SC-WACCM4; Smith et al., 2014) is employed to investigate the possible role of  
168 EsCB sea ice loss for the extreme low temperature events over western-central China.  
169 The horizontal resolution is  $1.9^\circ$  in latitude and  $2.5^\circ$  in longitude, and the vertical  
170 resolution has 66 levels extending up to 0.0006 hPa. The control experiments are  
171 performed with the climatological monthly SIC and SST averaged over 1982-2001  
172 (model-derived data) and other constant external forcings (greenhouse gases, aerosols,  
173 solar, etc.) at the year 2000 level. The sensitivity experiments are forced by decreased  
174 EsCB sea ice from August to October, calculated from composite detrended Arctic SIC  
175 with the detrended EsCB index greater than  $0.8\sigma$  (low sea ice: 1979, 1981, 1990, 2007,  
176 2008, 2012; [Figure S1b](#)). We only consider three months of sea ice forcing because  
177 significant signals with large anomalies mainly occur in August, September and  
178 October ([Figures S2a-c, h-j](#)). Sea ice loss from November to February is very weak  
179 with scattered significant regions ([Figure S2d-g, k-n](#)). Both, sensitivity and control  
180 experiments contain 100 members with different small perturbations added to the initial  
181 condition, running from August to February of the next year after the model spins up.  
182 The difference between the ensemble mean of the two experiments represents the  
183 atmospheric model responses to the prescribed EsCB sea ice loss, whose significance  
184 is examined by a two-tailed non-parametric Monte Carlo bootstrap significance test

185 (see more details in Ding and Wu, 2021).  
186



187

188 Figure 1 Regressed winter (a) 1000hPa air temperature (shading, unit: °C), (c)  
189 extreme low temperature frequency, and (e) 1000 (contour, unit: m) and 500 hPa  
190 (shading, unit: m) geopotential height anomalies on normalized autumn (September-  
191 October; SO) detrended EsCB index during 1979/80~2020/21. (b), (d), (f) same as (a),  
192 (c), (e), but for simulated results. Black dots indicate 90% confidence level. Black  
193 rectangles in (c) and (d) represent the range of western-central China (28°N–40°N,  
194 104°E–120°W).

195

196 **3. Results**

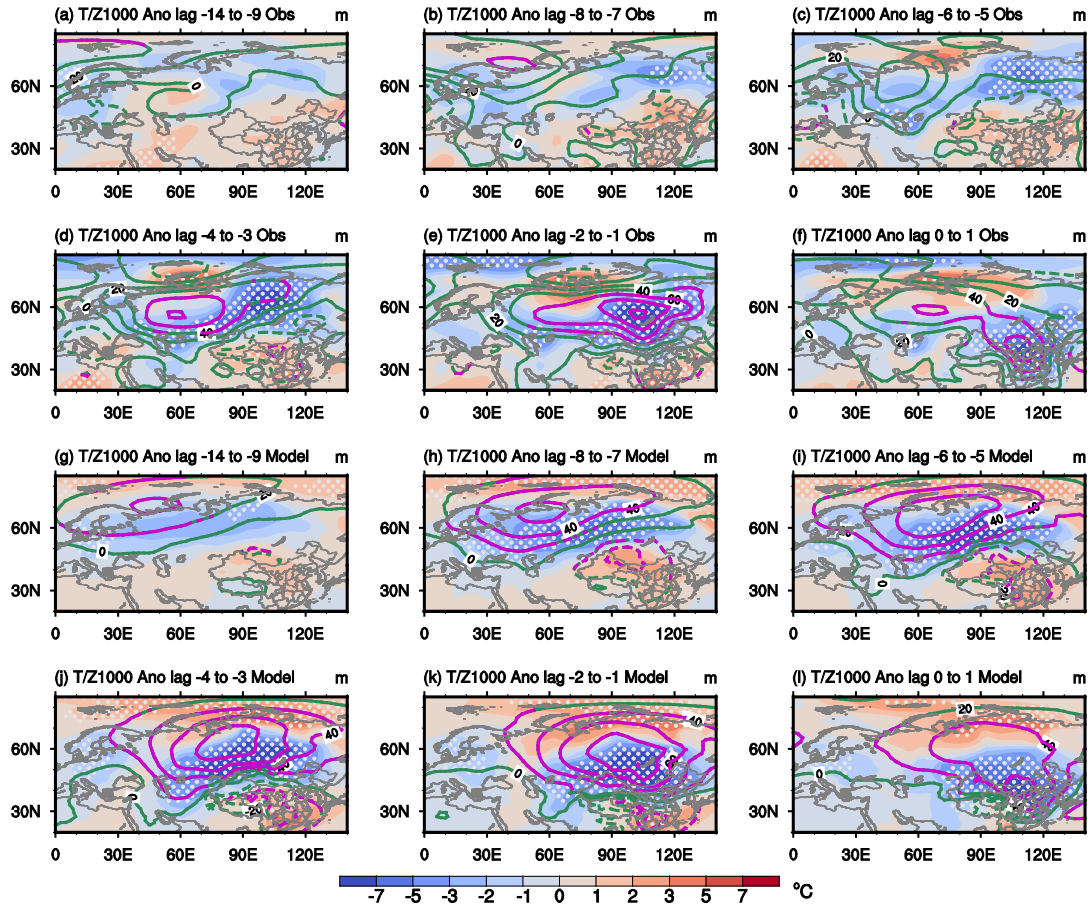
197 *3.1 Association between winter extreme low temperature and autumn sea ice loss*

198 The possible contribution of the autumn EsCB sea ice loss to winter temperature  
199 change anomalies over East Asia/China and associated Eurasian atmospheric  
200 circulation anomalies are displayed in [Figure 1](#), including the regression maps and  
201 simulated differences. The autumn EsCB sea ice loss shows a statistically weak link to  
202 the observed winter-mean cooling in most of China with limited significant range  
203 ([Figure 1a](#)). However, the reduced autumn EsCB sea ice statistically significantly  
204 favors an increase in the frequency of extreme low temperature events over western-  
205 central China (black box in [Figure 1c](#)). Compared to the climatological mean (10.71),  
206 in six reduced EsCB sea ice years, the area-mean frequency of extreme low temperature  
207 (13.83) over western-central China increases by 29.16% ( $p < 0.1$ ). The sea-ice sensitivity  
208 experiments confirm the above observed statistical association. In response to the  
209 prescribed autumn EsCB sea ice loss, the model produces relatively weak winter-mean  
210 cooling with limited significant range, but simultaneously exhibits a significantly  
211 increased frequency of winter extreme low temperature events over western-central  
212 China ([Figures 1b, d](#)). The simulated increased percentage (37.00%) for the frequency  
213 of winter extreme low temperature (12.33 versus 9) is close to the observations. Both,  
214 simulations and observations consistently show that autumn EsCB sea ice decrease can  
215 promote more frequent winter extreme low temperature events in western-central China.  
216 We hypothesize that atmospheric circulation anomalies associated with regional sea ice  
217 melt rapidly invade western-central China in a “pulse-like” manner causing a sudden  
218 drop in temperature for a limited time.

219 [Figure 2](#) shows composite maps of the evolution of air temperature and  
220 geopotential height anomalies at 1000hPa for observed and simulated extreme low  
221 temperature events in years with reduced SIC. Day 0 denotes the first day of extreme  
222 low temperature occurring in western-central China. On the day -14 ~ -9 (initial stage),  
223 cold anomalies already appear in northern Siberia (60°N–80°N), east of 60°E, together  
224 with positive geopotential height anomalies covering the Arctic region with a  
225 southward extension to the Greenland-Northern Europe sector ([Figures 2a, g](#)). During  
226 the next 6 days (developing stage), positive geopotential height anomalies gradually  
227 develop downstream and extend to Lake Baikal around 120°E, conducive to the  
228 accumulation and strengthening of cold anomalies over central Siberia (40°N–70°N,  
229 30°E–140°E; [Figures 2b-d, h-j](#)). Then, following the southward intrusion of the

230 Siberian anticyclonic anomaly, the significant cooling starts shifting southward on the  
231 day -2 ~ -1 and finally controls western-central China two days later (outbreak stage;  
232 20°N–60°N, 60°E–140°E), replacing the previous warm anomalies and leading to a  
233 sharp drop in temperature by 5~6 °C within 2~3 days (Figures 2e-f, k-l). In the middle  
234 troposphere, positive geopotential height anomalies cover the Arctic Ocean with  
235 southward extension to Northern Europe on the day -14 ~ -9 (Figures S3a, e), gradually  
236 strengthen toward the Ural Mountains within the subsequent 4 days (Figures S3b, f)  
237 and finally develop downstream to Lake Baikal from day -4 to day 1 (Figure S3c-d, g-  
238 h). To its southeast, significant negative geopotential height anomalies appear around  
239 Lake Baikal since day -8 ~ -5 through southeastward horizontal propagation of quasi-  
240 stationary planetary waves and shift toward the coast of East Asia about 6 days later.  
241 This middle tropospheric atmospheric configuration contributes to the Ural blocking  
242 high and strengthens the East Asian Trough. This provides favorable conditions for  
243 Arctic cold air invading western-central China. The pathway of the above cold  
244 anomalies mainly originates east of Novaya Zemlya southward to China (named the  
245 hyperpolar path in Bueh et al., 2022). To elucidate the main source and path of extreme  
246 low temperature, we further plot the count of cold anomalies < -5°C occurring in each  
247 Eurasian grid during the evolution of all extreme events based on the evolution  
248 characteristic of cold anomalies, including observed and simulated results (Figure 3a,  
249 b). Consistent with the former composite maps, when the autumn EsCB sea ice is  
250 reduced, the pathways of Arctic cold air inducing western-central China extreme low  
251 temperature events are dominated by the hyperpolar path (high frequency in deep red),  
252 with approximately 90% (10%) of the pathways deriving from the marginal seas to the  
253 east (west) of Novaya Zemlya (black dots in Figures 3a, b). Note, that winter air  
254 temperature in the climatological mean east of Novaya Zemlya is much colder, which  
255 explains that the hyperpolar path generally results in strong cooling in western-central  
256 China. Consequently, the downstream development of the anticyclonic anomaly over  
257 the Arctic Ocean-Northern Europe region is crucial for the rapid southward intrusion of  
258 Arctic cold air east of Novaya Zemlya into western-central China.

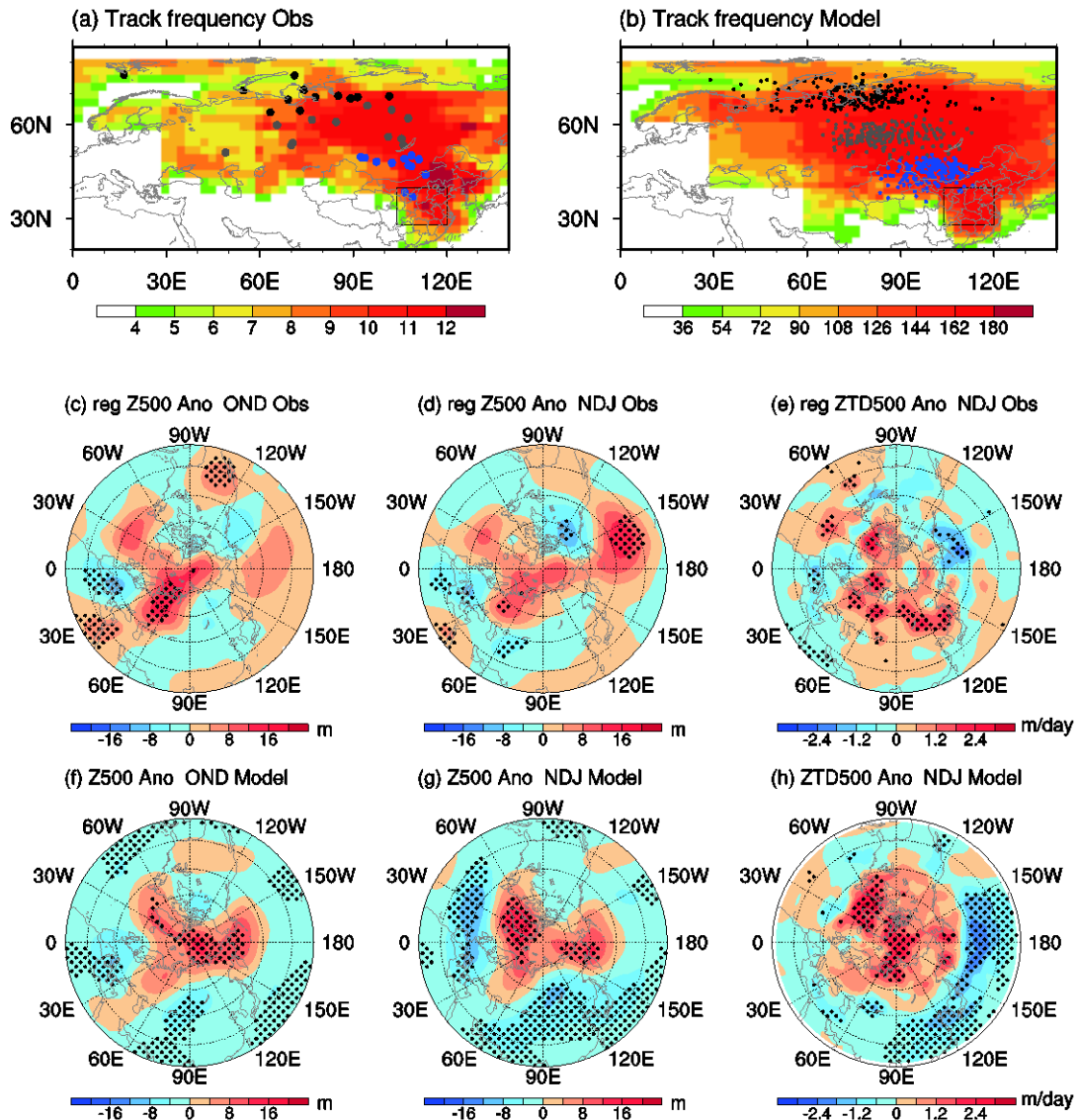
259



260

261 Figure 2 Composite evolution of detrended air temperature anomalies (shading,  
 262 unit: °C) and detrended geopotential height anomalies (green contour, unit: m) at 1000  
 263 hPa in (a) day -14 ~ -9, (b) day -8 ~ -7, (c) day -6 ~ -5, (d) day -4 ~ -3, (e) day -2 ~ -1 and  
 264 (f) day 0 ~ 1 for 12 extreme low temperature events over central-western China during  
 265 six low EsCB sea ice years. Day -14 ~ -9, with cold anomalies over northern Siberia, is  
 266 defined as the initial stage. Day -8 ~ -3, with cold anomalies over central Siberia, is  
 267 defined as the developing stage. Day -2 ~ 1, with cold anomalies over southern Siberia  
 268 and western-central China, is defined as the outbreak stage. (g) – (l) same as (a) - (f),  
 269 but for simulated results with 185 extreme low temperature events in 100 members.  
 270 Black dots and purple contours indicate 90% confidence level. The interval of contour  
 271 is 20 m.

272



273

274 Figure 3 (a) Count (shading) of extreme cold anomalies ( $< -5^{\circ}\text{C}$ ) occurring in each  
 275 Eurasian grid during the evolution of 12 observed extreme cold temperature events. We  
 276 divide the life cycle of extreme low temperature events into three stages covering the  
 277 distinct regions according to their evolution characteristics (Figure 2), including initial  
 278 (day-14  $\sim$  -9;  $60^{\circ}\text{N}$ – $80^{\circ}\text{N}$ ,  $0^{\circ}$ – $140^{\circ}\text{E}$ ), developing (day -8  $\sim$  -3;  $40^{\circ}\text{N}$ – $70^{\circ}\text{N}$ ,  $30^{\circ}\text{E}$ –  
 279  $140^{\circ}\text{E}$ ) and outbreak (day -2  $\sim$  1;  $20^{\circ}\text{N}$ – $60^{\circ}\text{N}$ ,  $60^{\circ}\text{E}$ – $140^{\circ}\text{E}$ ) stages. If grids in the  
 280 selected region appear cold anomalies less than  $-5^{\circ}\text{C}$  in either phase, we consider an  
 281 extreme low temperature event passing through these grids. Black, gray and blue dots  
 282 represent the mean location of cold anomalies  $< -5^{\circ}\text{C}$  in initial, developing, and  
 283 outbreak phases. The red shading and shift of dots represent the main pathway. Black  
 284 rectangles in (c) and (d) represent the range of western-central China. (b) same as (a),

285 but for simulated results with 185 extreme low temperature events. Regressed 500 hPa  
286 (c) late autumn (October-November-December) geopotential height anomalies  
287 (Shading, unit: m), (d) early winter (November-December-January) geopotential height  
288 anomalies (Shading, unit: m) and (e) early winter geopotential height tendency  
289 anomalies (Shading, unit:  $\text{m day}^{-1}$ ) on normalized SO detrended EsCB index. (f) - (h)  
290 same as (c) - (e), but for simulated results. Black dots in (c) - (h) indicate 90%  
291 confidence level.

292

293 The above anticyclonic anomaly also emerges in the winter-mean anomalous  
294 atmospheric circulation shown in [Figures 1e, f](#). As indicated by observations and  
295 simulations, the reduction of autumn EsCB sea ice makes the Arctic Ocean and  
296 Greenland-Northern Europe more prone to positive geopotential height anomalies from  
297 the lower to middle troposphere in winter. In the lower troposphere, positive  
298 geopotential height anomalies cover Northern Europe and expand eastward to East Asia.  
299 In the middle troposphere, a northwest-southeastward oriented dipole structure controls  
300 Eurasia with positive (negative) geopotential height anomalies over the Greenland-  
301 northern Ural Mountains (Lake Baikal) ([Figures 1e, f](#)). Such anomalous atmospheric  
302 configuration creates suitable background circulation (decelerated westerlies, reduced  
303 meridional potential vorticity gradient and enhanced meridional fluctuation of  
304 atmospheric circulation; Francis and Vavrus, 2015; Luo et al. 2018) for the intra-  
305 seasonal strengthening of the Siberian high ([Figure 2](#)), the Ural blocking high and the  
306 East Asian Trough ([Figure S2](#)), thus leading Arctic cold air rapidly to western-central  
307 China (hyperpolar path) and resulting in strong cooling within a few days.

308

### 309 *3.2 Possible mechanisms: the role of synoptic eddies and planetary waves*

310 Both, observations and simulations indicate that the increased frequency of  
311 extreme low temperature events over western-central China and the anticyclonic  
312 anomaly over the Arctic Ocean-Northern Europe are linked to the previous autumn  
313 EsCB sea ice loss. To elucidate the possible physical mechanisms, the evolution of  
314 observed and simulated 500 hPa geopotential height anomalies from one month after  
315 autumn EsCB sea ice minimum is examined. In late autumn (October-November-  
316 December), significant reduction of autumn regional sea ice increases the upward heat  
317 flux from the ocean (Ding et al. 2021; Ding and Wu, 2021) warming the Arctic

318 atmosphere and raising the geopotential height of the entire troposphere. Positive  
319 geopotential height anomalies control the Arctic region with southward extension in the  
320 North Atlantic sector (Figures 3c, f), then continue to develop and intensify southward  
321 in early winter (November-December-January) (Figures 3d, g). Its anomaly center  
322 finally moves to Greenland-Northern Europe one month later (Figures 1e, f). Previous  
323 works discovered that the local synoptic wave-mean flow interaction associated with  
324 the weakening (strengthening) of the North Atlantic storm track favors the generation  
325 of anticyclonic (cyclonic) forcing to the north (Ding et al., 2017, 2019). Here, we further  
326 calculated the geopotential height tendency. In early winter, observed and simulated  
327 positive geopotential height tendency anomalies dominate the Arctic region with  
328 significant and large anomalous signals around Greenland-Northern Europe (Figures  
329 3e, h). This indicates that the weakened North Atlantic storm track and associated  
330 interaction between synoptic waves and low-frequency flow contributes to the  
331 southward development and shift of the Arctic anticyclonic anomaly in the North  
332 Atlantic sector. In addition, the anomalous upward propagated quasi-stationary  
333 planetary wave energy related to the reduced autumn EsCB sea ice also supports the  
334 persistent Arctic positive geopotential height anomalies during mid-winter (Zhang et  
335 al., 2018b; Ding et al., 2021). In early winter, consistent with previous works (Ding and  
336 Wu, 2021), using a different model also confirms that planetary wave 2 dominates the  
337 increase in the upward propagation of quasi-stationary planetary wave energy, with two  
338 anomalous upward EP flux regions in the mid-high latitudes (Figures S4a-c). One  
339 upward branch propagates into the lower stratosphere and generates an EP flux  
340 convergence anomaly north of 60°N, leading to the decelerated westerly winds and  
341 weakened stratospheric polar vortex. The downward propagation of stratospheric  
342 anomalies favors the maintenance of the winter Arctic anticyclone anomaly and may  
343 provide a potential source for the downstream development of positive geopotential  
344 height anomalies around Northern Europe on the intra-seasonal timescale. Another  
345 upward branch converges poleward in the upper troposphere around 70°~80°N, directly  
346 strengthening the Arctic anticyclonic anomaly by wave-mean flow interaction.

347 As indicated in Figure 2, positive geopotential height anomalies over Northern  
348 Europe developing downstream are the vital system for the extreme low temperature  
349 outbreaks over western-central China. Consequently, we discuss the possible source of  
350 this atmospheric anomaly precursor based on time-height cross sections of observed  
351 and simulated area-mean geopotential height anomalies over the Ural Mountains (60°-

352 90°N, 40-80°E). Positive geopotential height anomalies, indicating the weakened polar  
353 vortex, control the lower-middle troposphere throughout the whole outburst of extreme  
354 low temperature air masses. Around day -10 ~ -9, the stratospheric anomalies begin to  
355 propagate downward and reach the lower-middle troposphere in the subsequent six days  
356 near the Ural Mountains (Figures S5a, b). This favors positive geopotential height  
357 anomalies in the troposphere expanding toward Lake Baikal. The timing of downward  
358 propagation is highly consistent with the timing (day -8~-3) of the enhancement and  
359 downstream development of anticyclonic anomaly around the Ural Mountains (Figures  
360 S3b-c, f-g). Therefore, the intra-seasonal downward propagation of planetary wave  
361 energy contributes to the Northern European anticyclonic anomaly downstream  
362 developing and supporting the Arctic cold air east of Novaya Zemlya to rapidly  
363 southward intrude western-central China (hyperpolar path).

364

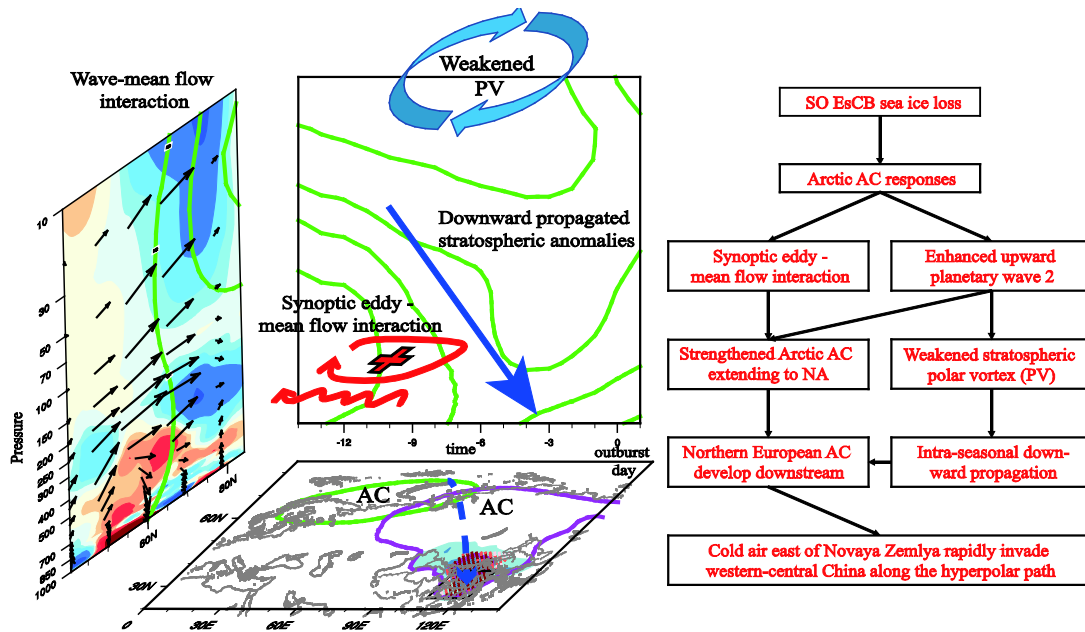
### 365 *3.3 Different impacts in comparison to Barents-Kara Sea ice*

366 Autumn sea ice variability in BK Seas, as the second EOF mode (Ding et al. 2021),  
367 is widely concerned and its climate role shows different feature compared with the  
368 EsCB sea ice loss. The sea ice loss exerts much stronger and more extensive impacts  
369 on winter-mean climate change, inducing significant cooling in most regions of China  
370 (Figures S6a, b) with stronger Siberian High and deeper East Asian Trough (Figures  
371 S6e, f; Wu et al., 2011). For the extreme low temperature, the significantly increased  
372 frequency mainly occurs in northwestern, northeastern and eastern China rather than in  
373 the western-central part (Figures S6c, d).

374 The Arctic-midlatitude association is non-stationary and varies with time under  
375 global warming (Chen et al., 2021; Wu et al., 2022), and similar results are obtained in  
376 our study (Figure S7a). The 19-year sliding correlation coefficients between the autumn  
377 EsCB index and the winter frequency of extreme low temperature over western-central  
378 China display significant positive correlations ( $r > 0.4$ ,  $p < 0.05$ ) since the late 1990s, with  
379 the highest value exceeding 0.7, indicating that the climate importance of EsCB sea ice  
380 change is increasingly evident. In contrast, the climate effects of BK sea ice anomalies  
381 on northwestern China are significant before the late 1990s ( $r > 0.4$ ,  $p < 0.05$ ) and have  
382 turned almost insignificant in recent two decades. The rapidly reduced climatological  
383 mean sea ice may modulate the above relationship (Chen et al., 2021).

384 In addition, the internal atmospheric variability can also interfere with the Arctic-  
385 midlatitude association. In the simulations, we further calculate the signal-to-noise ratio,

386 defined as the relative contributions induced by sea ice forcing to the model internal  
 387 variability. The increased frequency of winter extreme low temperature forced by EsCB  
 388 (BK) sea ice loss is about 30~40% of the model internal variability over western-central  
 389 (northeastern and eastern) China (Figure S7b, c). Therefore, the Arctic-midlatitudes  
 390 linkage is complex and non-stationary even if only considering the sea ice forcing.  
 391



392  
 393 Figure 4 Schematic diagram of the possible physical pathway for the reduced autumn  
 394 EsCB sea ice affecting the extreme low temperature events over western-central China.  
 395 AC and PV respectively indicate anticyclonic anomalies and polar vortex. Shadings in  
 396 the polar projection map, pressure-latitude map and latitude-longitude map represent  
 397 sea ice anomalies, EP flux divergence anomalies and 1000hPa air temperature  
 398 anomalies, respectively. Contours in all maps represent the geopotential height  
 399 anomalies. Purple (green) contours in the latitude-longitude map indicate the location  
 400 of Eurasian AC when (10 days before) the extreme cold outburst. Dots represent the  
 401 increased frequency of extreme low temperature. Blue dashed line arrow represents the  
 402 cold air outbreak path. Blue solid line arrow represents intra-seasonal downward  
 403 propagation of stratospheric anomalies. Vectors represent the EP flux. Curved arrow  
 404 represents the synoptic eddy - mean flow interaction and “+” with counterclockwise  
 405 arrow indicates positive geopotential height tendency anomalies.  
 406

#### 407 **4. Summary and Discussion**

408 By analyzing the reanalysis datasets and performing sea-ice sensitivity  
409 experiments, this study emphasizes the significant impact of autumn EsCB sea ice loss  
410 on climate change over western-central China. It is mainly reflected in the significantly  
411 increased frequency of winter extreme low temperature events rather than by winter-  
412 mean cooling. The specific physical processes are summarized in [Figure 4](#). When the  
413 previous autumn EsCB sea ice is reduced, enhanced heat flux upward from the open  
414 water results in significant local warming and elevation of geopotential height levels  
415 controlling the Arctic troposphere one month later. Then, under the influence of two  
416 possible mechanisms, the positive geopotential potential height anomalies persist into  
417 winter. One possible mechanism is the local synoptic eddy-mean flow interaction  
418 associated with the weakened North Atlantic storm track that facilitates the Arctic  
419 anticyclonic anomaly developing southward with the anomalous center shifting to  
420 Greenland-Northern Europe. The other possible mechanism is associated with the  
421 anomalous upward propagation of quasi-stationary planetary waves and its generated  
422 wave-mean flow interaction (EP flux convergence anomaly), dominated by planetary  
423 wave 2. The tropospheric branch directly strengthens the Arctic positive geopotential  
424 height anomalies in early winter. The stratospheric branch attenuates the winter polar  
425 vortex, favoring the intra-seasonal downward propagation of stratospheric anomalies  
426 and contributing to the persistent Arctic anticyclonic anomaly throughout the entire  
427 troposphere. Therefore, Greenland-Northern Europe is generally dominated by positive  
428 geopotential anomalies in the wintertime. When the stratospheric anomalies propagate  
429 downward on the intra-seasonal timescale, the Northern European positive geopotential  
430 anomalies strengthen and develop downstream within 7 days, which favors severe  
431 Arctic cold air east of Novaya Zemlya shifting southward (hyperpolar path) and  
432 accumulating in Siberia around Lake of Baikal. In the subsequent 2~3 days, these cold  
433 anomalies rapidly invade western-central China, bringing a sudden sharp drop in  
434 temperature and explaining the increased frequency of extreme low temperature there.  
435 The climate role of autumn EsCB sea ice change in western-central China has become  
436 increasingly significant in recent two decades. In contrast, autumn sea ice loss in BK  
437 Seas favors more frequent extreme low temperature events over northeastern and  
438 eastern China, whose dominant effects occur before the late 1990s.

439 Although the simulations capture the main features of the observations, certain  
440 simulated deviations still exist. For example, the location of the simulated winter-mean

441 Arctic anticyclonic anomaly is farther north than the observed. On intra-seasonal  
442 timescale, compared to observations, the simulated Siberian cold anomalies from day -  
443 14 to day -5 shift eastward and are more significant, accompanied by stronger positive  
444 geopotential height anomalies over northern Eurasian. These simulated deviations may  
445 be related to the inaccurate model descriptions and lack of other external forcings such  
446 as Eurasian snow cover and sea surface temperature in Pacific or Atlantic Ocean.  
447 Besides downward propagating stratospheric signals, other factors such as the intra-  
448 seasonal oscillation may also trigger the downstream development of Northern  
449 European anticyclonic anomaly. These phenomena are out of scope of our discussion.  
450 In addition, favorable initial atmospheric conditions or internal atmospheric variability  
451 for autumn EsCB sea ice affecting extreme low temperature in China needs further  
452 investigation.

453

#### 454 **Acknowledgments**

455 This study is supported jointly by the State Key Program of National Natural Science  
456 of China (Grant 41730959), the National Key Basic Research Project of China (Grant  
457 2019YFA0607002), the Major Program of the National Natural Science Foundation of  
458 China (Grant 41790472), and the National Natural Science Foundation of China (Grant  
459 41905058).

460

#### 461 **Open Research**

462 The Monthly mean sea ice concentration (SIC) from the Met Office Hadley Center are  
463 available via <https://www.metoffice.gov.uk/hadobs/hadisst/data/download.html>. The  
464 NCEP-NCAR (National Center for Environmental Prediction) - DOE (Department of  
465 Energy) Reanalysis II dataset is available at  
466 <https://psl.noaa.gov/data/gridded/data.ncep.reanalysis2.html>.

467

#### 468 **Reference**

469 Barnes EA (2013) Revisiting the evidence linking Arctic amplification to extreme  
470 weather in midlatitudes. *Geophys Res Lett* 40: 4734–4739. [https://doi.org/  
471 10.1002/grl.50880](https://doi.org/10.1002/grl.50880)  
472 Bueh C, Peng JB, Lin DW, Chen BM (2022) On the Two Successive Supercold Waves  
473 Straddling the End of 2020 and the Beginning of 2021, *Adv Atmos Sci*. doi:

474 10.1007/s00376-021-1107-x

475 Blackport R, Screen JA, van der Wiel K, Bintanja R (2019) Minimal influence of  
476 reduced Arctic sea ice on coincident cold winters in mid-latitudes. *Nat Climate*  
477 *Change* 9: 697–704. <https://doi.org/10.1038/s41558-019-0551-4>.

478 Blackport R, Screen JA (2020) Insignificant effect of Arctic amplification on the  
479 amplitude of midlatitude atmospheric waves. *Sci Adv* 6: eaay2880. [https://doi.org/](https://doi.org/10.1126/sciadv.aay2880)  
480 [10.1126/sciadv.aay2880](https://doi.org/10.1126/sciadv.aay2880)

481 Blackport R, Screen JA (2021) Observed Statistical Connections Overestimate the  
482 Causal Effects of Arctic Sea Ice Changes on Midlatitude Winter Climate. *J Climate*  
483 34(8): 3021–3038.

484 Cai M, Yang S, Van Den Dool HM, Kousky VE (2007) Cai M, Yang S, Van Den Dool  
485 H M, et al. Dynamical implications of the orientation of atmospheric eddies: A  
486 local energetics perspective[J]. *Tellus A: Dynamic Meteorology and*  
487 *Oceanography*, 2007, 59(1): 127-140.

488 Chen HW, Zhang F, Alley RB (2016a) The robustness of midlatitude weather pattern  
489 changes due to Arctic sea ice loss. *J Climate* 29: 7831–7849.  
490 <https://doi.org/10.1175/JCLI-D-16-0167.1>.

491 Chen HW, Alley RB, Zhang F (2016b) Interannual Arctic sea ice variability and  
492 associated winter weather patterns: A regional perspective for 1979–2014. *J*  
493 *Geophys Res Atmos* 121(14): 433–455. [https://doi.org/10.1002/](https://doi.org/10.1002/2016JD024769) [2016JD024769](https://doi.org/10.1002/2016JD024769)

494 Chen S, Wu R, Chen W, Song L, Cheng W, Shi W (2021) Weakened impact of autumn  
495 Arctic sea ice concentration change on the subsequent winter Siberian High  
496 variation around the late - 1990s. *Int J Climatol*, 41, E2700-E2717.

497 Chen W, Graf HF, Takahashi M (2002) Observed interannual oscillations of planetary  
498 wave forcing in the Northern Hemisphere winter. *Geophys Res Lett* 29: 2073.  
499 <https://doi.org/10.1029/2002GL016062>

500 Chen W, Takahashi M, Graf HF (2003) Interannual variations of stationary planetary  
501 wave activity in the northern winter troposphere and stratosphere and their  
502 relations to NAM and SST. *J Geophys Res* 108: 4797. [https://doi.org/10.1029/](https://doi.org/10.1029/2003JD003834)  
503 [2003JD003834](https://doi.org/10.1029/2003JD003834)

504 Cohen J, Zhang X, Francis J, et al (2020) Divergent consensus on Arctic amplification  
505 influence on midlatitude severe winter weather. *Nat Climate Change* 10: 20–29.  
506 <https://doi.org/10.1038/s41558-019-0662-y>

507 Cohen J, Agel L, Barlow M, Garfinkel CI, White I (2021) Linking Arctic variability  
508 and change with extreme winter weather in the United States. *Science*, 373(6559),  
509 1116-1121. DOI: 10.1126/science.abi9167.

510 Deng J, Dai A (2022) Sea ice–air interactions amplify multidecadal variability in the  
511 North Atlantic and Arctic region. *Nat Commun* 13, 2100.  
512 <https://doi.org/10.1038/s41467-022-29810-7>

513 Deser C, Magnusdottir G, Saravanan R, Phillips A (2004) The effects of North Atlantic  
514 SST and sea-ice anomalies on the winter circulation in CCM3. Part II: Direct and  
515 indirect components of the response. *J Climate* 17: 877–889. [https://doi.org/](https://doi.org/10.1175/1520-0442(2004)017,0877:TEONAS.2.0.CO;2)  
516 [10.1175/1520-0442\(2004\)017,0877:TEONAS.2.0.CO;2](https://doi.org/10.1175/1520-0442(2004)017,0877:TEONAS.2.0.CO;2)

517 Ding S, Chen W, Feng J, Graf HF (2017) Combined impacts of PDO and two types of  
518 La Niña on climate anomalies in Europe. *J Climate* 30(9).

519 Ding S, Chen W, Graf HF, Chen Z, Ma T (2019) Quasi-stationary extratropical wave  
520 trains associated with distinct tropical Pacific seasonal mean convection patterns:  
521 observational and AMIP model results. *Clim Dyn*, 53: 2451-2476.

522 Ding S, Wu B (2021) Linkage between autumn sea ice loss and ensuing spring Eurasian  
523 temperature. *Clim Dyn*, 57(9), 2793-2810. [https://doi.org/10.1007/s00382-021-](https://doi.org/10.1007/s00382-021-05839-0)  
524 [05839-0](https://doi.org/10.1007/s00382-021-05839-0).

525 Ding S, Wu B, Chen W (2021) Dominant Characteristics of Early Autumn Arctic Sea  
526 Ice Variability and Its Impact on Winter Eurasian Climate. *J Clim*, 34(5), 1825-  
527 1846. <https://doi.org/10.1175/JCLI-D-19-0834.1>.

528 Edmon H, Hoskins BJ, McIntyre ME (1980) Eliassen–Palm cross sections for the  
529 troposphere. *J Atmos Sci* 37: 2600–2616. [https://doi.org/10.1175/1520-0469\(1980\)](https://doi.org/10.1175/1520-0469(1980)037,2600:EPCSFT.2.0.CO;2)  
530 [037,2600:EPCSFT.2.0.CO;2](https://doi.org/10.1175/1520-0469(1980)037,2600:EPCSFT.2.0.CO;2)

531 Francis JA, Chan W, Leathers DJ, Miller JR, Veron DE (2009) Winter Northern  
532 Hemisphere weather patterns remember summer Arctic sea-ice extent. *Geophys*  
533 *Res Lett* 36: L07503. <https://doi.org/10.1029/2009GL037274>

534 Francis JA, Vavrus SJ (2012) Evidence linking Arctic amplification to extreme weather  
535 in mid-latitudes. *Geophys. Res. Lett.*, 39, L06801,  
536 <https://doi.org/10.1029/2012GL051000>.

537 Francis JA, Vavrus SJ (2015) Evidence for a wavier jet stream in response to rapid  
538 Arctic warming. *Environ Res Lett* 10: 014005. [https://doi.org/10.1088/1748-](https://doi.org/10.1088/1748-9326/10/1/014005)  
539 [9326/10/1/014005](https://doi.org/10.1088/1748-9326/10/1/014005)

540 Honda M, Inoue J, Yamane S (2009) Influence of low Arctic sea-ice minima on  
541 anomalously cold Eurasian winters. *Geophys Res Lett* 36: L08707. [https://doi.org/](https://doi.org/10.1029/2008GL037079)  
542 [10.1029/2008GL037079](https://doi.org/10.1029/2008GL037079)

543 Kanamitsu M, Ebisuzaki W, Woollen J, Yang SK, Hnilo JJ, Fiorino M, Potter GL (2002)  
544 NCEP-DOE AMIP-II Reanalysis (R-2). *Bull Amer Meteor Soc* 83: 1631–1643.  
545 <https://doi.org/10.1175/BAMS-83-11-1631>

546 Koenigk T, Gao Y, Gastineau G, et al (2019) Impact of Arctic sea ice variations on  
547 winter temperature anomalies in Northern Hemispheric land areas. *Climate Dyn*  
548 52: 3111–3137. <https://doi.org/10.1007/s00382-018-4305-1>

549 Lau NC, Holopainen EO (1984) Transient eddy forcing of the time-mean flow as  
550 identified by geopotential tendencies. *J Atmos Sci* 41: 313–328

551 Lau NC (1988) Variability of the observed midlatitude storm tracks in relation to low-  
552 frequency changes in the circulation pattern. *J Atmos Sci* 45: 2718–2743

553 Lau NC, Nath MJ (1991) Variability of the baroclinic and barotropic transient eddy  
554 forcing associated with monthly changes in the midlatitude storm tracks. *J Atmos*  
555 *Sci* 48: 2589–2613

556 Luo D, Chen X, Dai A, Simmonds I (2018) Changes in atmospheric blocking  
557 circulations linked with winter Arctic warming: A new perspective. *J Climate*,  
558 31(18): 7661-7678.

559 McCusker KE, Fyfe JC, Sigmond M (2016) Twenty-five winters of unexpected  
560 Eurasian cooling unlikely due to Arctic sea-ice loss. *Nat Geosci* 9: 838–842.  
561 <https://doi.org/10.1038/ngeo2820>

562 Mori M, Watanabe M, Shiogama H, Inoue J, Kimoto M (2015) Robust Arctic sea-ice  
563 influence on the frequent Eurasian cold winters in past decades. *Nat Geosci* 7:

564 869–873. <https://doi.org/10.1038/ngeo2277>

565 Mori M, Kosaka Y, Watanabe M, Nakamura H, Kimoto M (2019) A reconciled estimate  
566 of the influence of Arctic sea-ice loss on recent Eurasian cooling. *Nat Climate*  
567 *Change* 9: 123–129. <https://doi.org/10.1038/s41558-018-0379-3>

568 Nakamura T, Yamazaki K, Sato T, Ukita J (2019) Memory effects of Eurasian land  
569 processes cause enhanced cooling in response to sea ice loss. *Nat Commun* 10:  
570 5111. <https://doi.org/10.1038/s41467-019-13124-2>

571 Overland JE, Ballinger TJ, Cohen J, Francis JA, Hanna E, Jaiser R, et al. (2021) How  
572 do intermittency and simultaneous processes obfuscate the Arctic influence on  
573 midlatitude winter extreme weather events? *Environ Res Lett*, 16(4), 043002.

574 Petoukhov V, Semenov V (2010) A link between reduced Barents–Kara sea ice and cold  
575 winter extremes over northern continents. *J Geophys Res* 115: D21111.  
576 <https://doi.org/10.1029/2009JD013568>

577 Plumb RA (1985) On the three-dimensional propagation of stationary waves. *J Atmos*  
578 *Sci* 42: 217–229. [https://doi.org/10.1175/1520-0469\(1985\)042.0217:  
579 OTTDPO.2.0.CO;2](https://doi.org/10.1175/1520-0469(1985)042<0217:OTTDPO.2.0.CO;2)

580 Rayner NA, Parker DE, Horton EB, Folland CK, Alexander LV, Rowell DP, Kent EC,  
581 Kaplan A (2003) Global analyses of sea surface temperature, sea ice, and night  
582 marine air temperature since the late nineteenth century. *J Geophys Res* 108: 4407.  
583 <https://doi.org/10.1029/2002JD002670>

584 Screen JA (2017) Simulated atmospheric response to regional and pan-Arctic sea ice  
585 loss. *J Climate* 30: 3945–3962. <https://doi.org/10.1175/JCLI-D-16-0197.1>

586 Siew PYF, Li C, Sobolowski SP, King MP (2020) Intermittency of Arctic-mid-latitude  
587 teleconnections: stratospheric pathway between autumn sea ice and the winter  
588 North Atlantic Oscillation. *Weather Clim Dyn*, 1(1), 261–275.  
589 <https://doi.org/10.5194/wcd-1-261-2020>.

590 Smith KL, Neely RR, Marsh DR, Polvani LM (2014) The Specified Chemistry Whole  
591 Atmosphere Community Climate Model (SC-WACCM). *J Adv Model Earth Syst*,  
592 6, 883–901, <https://doi.org/10.1002/2014MS000346>.

593 Sun L, Perlwitz J, Hoerling M (2016) What caused the recent “warm Arctic, cold

594 continents” trend pattern in winter temperatures? *Geophys Res Lett* 43: 5345–  
595 5352. <https://doi.org/10.1002/2016GL069024>

596 Tang QH, Zhang X, Yang X, Francis JA (2013) Cold winter extremes in northern  
597 continents linked to Arctic sea ice loss. *Environ Res Lett* 8: 014036.  
598 <https://doi.org/10.1088/1748-9326/8/1/014036>

599 Vihma T (2014) Effects of Arctic sea ice decline on weather and climate: A review. *Surv*  
600 *Geophys* 35: 1175–1214. <https://doi.org/10.1007/s10712-014-9284-0>

601 Wu B, Su J, Zhang R (2011) Effects of autumn-winter Arctic sea ice on winter Siberian  
602 high. *Chin Sci Bull* 56: 3220–3228. <https://doi.org/10.1007/s11434-011-4696-4>

603 Wu B, Handorf D, Dethloff K, Rinke A, Hu A (2013) Winter weather patterns over  
604 northern Eurasia and Arctic sea ice loss. *Mon Wea Rev* 141: 3786–3800.  
605 <https://doi.org/10.1175/MWR-D-13-00046.1>

606 Wu B, Yang K, Francis JA (2017) A cold event in Asia during January–February 2012  
607 and its possible association with arctic sea ice loss. *J Climate* 30: 7971–7990.  
608 <https://doi.org/10.1175/JCLI-D-16-0115.1>

609 Wu B, Li ZK, Francis JA, Ding S (2022) A recent weakening of winter temperature  
610 association between Arctic and Asia. *Environ Res Lett*, doi:10.1088/1748-  
611 9326/ac4b51.

612 Zhang P, Wu Y, Smith KL (2018a) Prolonged effect of the stratospheric pathway in  
613 linking Barents–Kara Sea sea ice variability to the midlatitude circulation in a  
614 simplified model. *Climate Dyn* 50: 527–539. [https://doi.org/10.1007/s00382-017-  
615 3624-y](https://doi.org/10.1007/s00382-017-3624-y)

616 Zhang P, Wu Y, Simpson IR, Smith KL, Zhang X, De B, Callaghan P (2018b) A  
617 stratospheric pathway linking a colder Siberia to Barents-Kara Sea sea ice loss.  
618 *Sci Adv* 4: eaat6025. <https://doi.org/10.1126/sciadv.aat6025>

619 Zhang RN, Screen JA, Zhang RH (2022) Arctic and Pacific Ocean Conditions Were  
620 Favourable for Cold Extremes over Eurasia and North America during Winter  
621 2020/21. *Bulletin of the American Meteorological Society*, DOI: 10.1175/BAMS-  
622 D-21-0264.1

623